

## Time-dependent 3-D Multi-physics Simulation of the Passively Autonomous Daily Load-follow in ATOM SMR

Ahmed Amin E. Abdelhameed, and Yonghee Kim\*  
Department of Nuclear & Quantum Engineering  
Korea Advanced Institute of Science and Technology  
291 Daehak-ro Yuseong-gu, Daejeon, Korea, 34141  
\*Corresponding author: [yongheekim@kaist.ac.kr](mailto:yongheekim@kaist.ac.kr)

### 1. Introduction

The passively autonomous load-follow operation aims at achieving load-follow operation without any reactivity control by the control rods or soluble boron. Previously, we illustrated the feasibility of the passively autonomous frequency control operation and fast load-follow scenarios [1]. In this paper, we demonstrate the physics of slow daily load-follow operation through 3D time-dependent simulation of two days a typical 100-50-100 pattern. The numerical simulations are carried out for the 450 MWth ATOM SMR. ATOM achieves a high performance soluble-boron-free (SBF) operation by radial zoning of the CSBA burnable absorbers [2]. Figure 1 shows a schematic of ATOM core design. Whole core time-dependent neutronic and thermal-hydraulic simulations are coupled with a time-dependent model of a helical coil steam generator (HCSG). The results of this work demonstrate a successful passively autonomous load-follow.

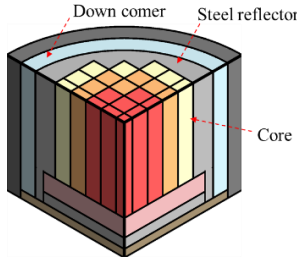


Fig. 1. Quarter ATOM core

### 2. Methods

In the numerical simulations, the feed water to the secondary of the HCSG is adjusted to extract the demanded power from the primary loop. Figure 2 shows schematic of the system model. The variation of the heat transfer to the secondary side, varies the core inlet coolant temperature. Because the moderator temperature coefficient (MTC) is strongly negative in the SBF ATOM core from BOC, it governs the core power maneuvering to follow the power demand. MTC is about -48 pcm/K at BOC and becomes more negative with depletion [2]. Meanwhile, the variation of the core average coolant temperature remains rather limited. Figure 3 illustrates the time-dependent system models that are solved by an in-house FORTRAN code. In the algorithm, the 3-D transient NEM solution is coupled with the dynamic Xe and Sm, as well as, the heat transfer in all fuel channels.

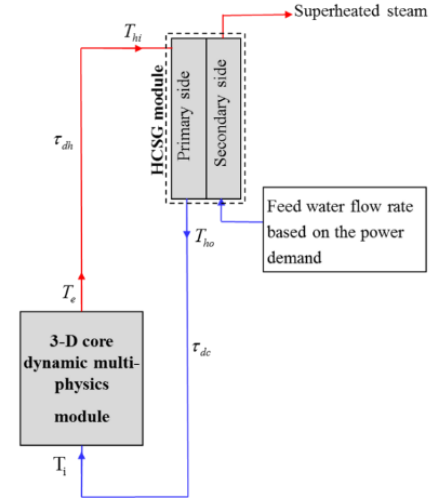


Fig. 2. Schematic of the system model

The 3-D neutronic solution is based on NEM method with one node scheme. In nodal methods, by integrating the time-dependent multi-group diffusion equation over the node volume, as shown in Eq. 1, the node balance equation is obtained as given in Eq. 2. Obtaining the surface currents is required to solve Eq. 2 and a common practice is to integrate the partial differential equation of the 3-D neutron flux over the two directions transverse to each coordinate. In NEM, the neutron flux is approximated using a 4th order polynomial. It should be noticed that the discontinuity of the homogenous surface flux should be represented in the flux coefficients and the coefficients that appear in out-going partial currents update as given in Eqs. 3-7 [3]. The thermal-hydraulic module solves the time-dependent balance equations of mass, energy, and axial momentum as shown in Eqs. 8-10.

$$\begin{aligned}
 & \int_{-\Delta x/2}^{\Delta x/2} \int_{-\Delta y/2}^{\Delta y/2} \int_{-\Delta z/2}^{\Delta z/2} \frac{1}{v_g} \frac{\partial \phi_g^\sigma}{\partial t} dx dy dz \\
 & + \int_{-\Delta x/2}^{\Delta x/2} \int_{-\Delta y/2}^{\Delta y/2} \int_{-\Delta z/2}^{\Delta z/2} \left[ \frac{\partial}{\partial x} J_{sx}^\sigma + \frac{\partial}{\partial y} J_{sy}^\sigma + \frac{\partial}{\partial z} J_{sz}^\sigma + \sum_{r \neq g} \phi_r^\sigma \right] dx dy dz = \\
 & \int_{-\Delta x/2}^{\Delta x/2} \int_{-\Delta y/2}^{\Delta y/2} \int_{-\Delta z/2}^{\Delta z/2} \sum_{g'=1}^G [\sum_{s \neq g} \sigma_{s \rightarrow g} + (1-\beta) \frac{X_{gp}}{K} v \sum_{f \neq g} \phi_f^\sigma] \phi_g^\sigma dx dy dz \\
 & + \int_{-\Delta x/2}^{\Delta x/2} \int_{-\Delta y/2}^{\Delta y/2} \int_{-\Delta z/2}^{\Delta z/2} \sum_{i=1}^I X_{dgi} \lambda_i c_i dx dy dz \\
 & \left[ \frac{1}{v_g} \frac{\partial}{\partial t} + \sum_{u=x,y,z} \frac{1}{h_u} [(J_{gu}^{\sigma-} + J_{gu}^{\sigma+}) - (J_{gu}^{\sigma+} + J_{gu}^{\sigma-})] + \sum_{r \neq g} \overline{\Phi}_r^\sigma \right] \Phi_g^\sigma = \\
 & \sum_{g'=1}^G [\sum_{s \neq g} \sigma_{s \rightarrow g} + (1-\beta) \frac{X_{gp}}{K} v \sum_{f \neq g} \overline{\Phi}_f^\sigma] \Phi_g^\sigma + \sum_{i=1}^I X_{dgi} \lambda_i c_i
 \end{aligned} \quad (1)$$

$$\left[ \frac{1}{v_g} \frac{\partial}{\partial t} + \sum_{u=x,y,z} \frac{1}{h_u} [(J_{gu}^{\sigma-} + J_{gu}^{\sigma+}) - (J_{gu}^{\sigma+} + J_{gu}^{\sigma-})] + \sum_{r \neq g} \overline{\Phi}_r^\sigma \right] \Phi_g^\sigma = \quad (2)$$

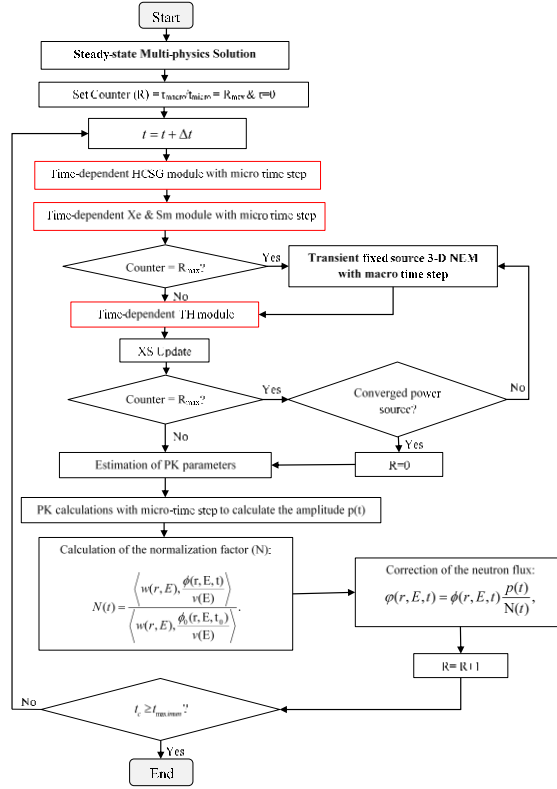


Fig. 3. PCQM algorithm in the in-house 3D system code

For each axial node, the fuel heat transfer module solves the heat conduction equation, which is given in Eq. 11, in the radial direction for discretized nodes. In the HCSG module, the time-dependent thermal-hydraulics solutions for both primary and secondary sides are performed based on known power demand and flow rates. During the iterations, the power profile is updated using Eq.12. Moreover, in order to reduce the cost of the time-dependent 3-D solution, the predictor corrector quasi-static method (PCQM) is used. In PCQM, the neutron flux is factorized to its shape and amplitude parts as given in Eq.13. The predicted shape function is used to obtain the point kinetic (PK) parameters for the macro step. Then, the PK equation is solved with a smaller time step to correct the amplitude of the neutron flux as given in Eq.14 [1].

$$a_{g0}^{\sigma} = \overline{\Phi_g^{\sigma}} \quad (3)$$

$$a_{gu1}^{\sigma} = \frac{\Phi_{gur}^{\sigma}}{F_{gur}} - \frac{\Phi_{gul}^{\sigma}}{F_{gul}} \quad (4)$$

$$a_{gu2}^{\sigma} = 3 \left( \frac{\Phi_{gur}^{\sigma}}{F_{gur}} + \frac{\Phi_{gul}^{\sigma}}{F_{gul}} - 2\overline{\Phi_g^{\sigma}} \right) \quad (5)$$

$$J_{gul}^{out,\sigma} = C_{0gul} \overline{\Phi_g^{\sigma}} + C_{1gul} J_{gul}^{in,\sigma} + C_{2gul} J_{gur}^{in,\sigma} + C_{3gul} a_{gu3}^{\sigma} - C_{4gul} a_{gu4}^{\sigma} \quad (6)$$

$$J_{gur}^{out,\sigma} = C_{0gur} \overline{\Phi_g^{\sigma}} + C_{2gur} J_{gul}^{in,\sigma} + C_{1gur} J_{gur}^{in,\sigma} - C_{3gur} a_{gu3}^{\sigma} - C_{4gur} a_{gu4}^{\sigma} \quad (7)$$

where

$$\mu_{gu} = \frac{D_g}{\Delta u},$$

$$M_{gu} = F_{gul} F_{gur} + 8\mu_{gu} F_{gul} + 8\mu_{gu} F_{gur} + 48\mu_{gu}^2,$$

$$C_{0gul} = \frac{6\mu_{gu} F_{gul} (F_{gur} + 4\beta)}{M_{gu}}, C_{0gur} = \left( \frac{6\mu_{gu} F_{gur} (4\mu_{gu} + F_{gul})}{M_{gu}} \right),$$

$$C_{1gul} = \frac{F_{gul} F_{gur} + 8\mu_{gu} F_{gul} - 8\mu_{gu} F_{gur} - 48\mu_{gu}^2}{M_{gu}},$$

$$C_{1gur} = \left( \frac{F_{gul} F_{gur} - 8\mu_{gu} F_{gul} + 8\mu_{gu} F_{gur} - 48\mu_{gu}^2}{M_{gu}} \right),$$

$$C_{2gul} = \frac{-8\mu_{gu} F_{gul}}{M_{gu}}, C_{2gur} = \left( \frac{-8\mu_{gu} F_{gur}}{M_{gu}} \right),$$

$$C_{3gul} = \left( \frac{\mu_{gu} F_{gul} (F_{gur} + 12\mu_{gu})}{2M_{gu}} \right), C_{3gur} = \left( \frac{\mu_{gu} F_{gur} (F_{gul} + 12\mu_{gu})}{2M_{gu}} \right),$$

$$C_{4gul} = \left( \frac{\mu_{gu} F_{gul} (F_{gur} + 4\mu_{gu})}{5M_{gu}} \right), C_{4gur} = \left( \frac{\mu_{gu} F_{gur} (F_{gul} + 4\mu_{gu})}{5M_{gu}} \right).$$

$$A_i \frac{\partial \rho_i}{\partial t} + \frac{\Delta m_i}{\Delta z_i} = 0, \quad (8)$$

$$A_i \frac{\partial (\rho_i h_i)}{\partial t} + \frac{\Delta (m_i h_i)}{\Delta z_i} = q_i, \quad (9)$$

$$\frac{\partial m_i}{\partial t} + \frac{\Delta (m_i v_i)}{\Delta z_i} = -A_i \rho_i g_i - A_i \frac{\Delta P_i}{\Delta z_i} - \frac{F_i}{\Delta z_i}, \quad (10)$$

$$\rho_j C_{p,j} V_j \frac{\partial T_j}{\partial t} = Q_j V_j + Q_{j-1,j} + Q_{j+1,j} \quad (11)$$

$$Q_i = \frac{T_{pr,i} - T_{sc,i}}{\left( \frac{1}{H_{pr,i} A_{pr,i}} \right) + \left( \frac{1}{H_{sc,i} A_{sc,i}} \right) + \left( \frac{\tau}{K_{t,i} A_{t,i}} \right)}. \quad (12)$$

$$\phi(r, E, t) = p(t) \psi(r, E, t). \quad (13)$$

$$\frac{dp(t)}{dt} = \frac{\rho(t) - \beta(t)}{\Lambda} p(t) + \sum_k \lambda_k C_k(t), \quad (14)$$

$$\frac{dC_k(t)}{dt} = -\lambda_k C_k(t) + \frac{\beta_k}{\Lambda} p(t), k = 1, 2, \dots, 6, \quad (15)$$

where

$$\rho(t) = 1 - \frac{K_0}{K(t)},$$

$$K(t) = \frac{\langle w(r, E), \chi_p(E) F \Psi(r, E, t) \rangle}{\langle w(r, E), (L + R - S) \Psi(r, E, t) \rangle},$$

$$\beta_k(t) = \frac{\langle w(r, E), \chi_k(E) \beta_k F \Psi(r, E, t) \rangle}{\langle w(r, E), \chi_p(E) F \Psi(r, E, t) \rangle},$$

$$\Lambda(t) = \frac{\langle w(r, E), -\frac{1}{v(E)} \Psi(r, E, t) \rangle}{\langle w(r, E), \frac{1}{k_0} \chi_p(E) F \Psi(r, E, t) \rangle}.$$

### 3. Results and Discussions

This section demonstrates the results of transient 3-D neutronic-TH coupled simulation in the core coupled with the primary and secondary transient TH models of the HCSG. The PCQM iterations are performed with 11 sec macro-time step and 0.1 sec micro-time step. The passively autonomous load-follow simulation in ATOM starts from steady state hot full power (HFP) condition after Xe equilibrium. The simulation is carried out at BOC condition where the excess reactivity in the core is compensated for by the control element assemblies. It should be noticed that in ATOM the least MTC value in the cycle occurs at BOC. However, the power maneuvering is obtained entirely due to the strongly negative MTC in ATOM. Figure 4 shows the variation of the feed water flow rate to the secondary of the HCSGs during two days of 100-50-100 load patterns.

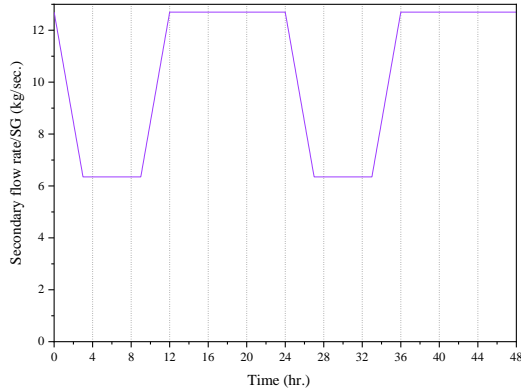


Fig. 4. Feed water flow rate to HCSG secondary

For the power demand ramp-down phase, less heat is extracted from the primary loop. Thus, the core inlet coolant temperature ( $T_i$ ) increases as shown in Fig. 5. The core coolant temperatures plotted in Fig. 5 are averaged over the 69 fuel assembly channels of the ATOM core. The increase in  $T_i$  leads to a negative coolant-induced reactivity feedback. Therefore, the core power starts to decrease following the decrease in the power demand. Xe concentration slowly increases during the 1st power ramp-down phase, which enhances the power ramping down and reduces the deviation of the core average coolant temperature ( $T_a$ ). Meanwhile, fuel temperature decreases as the reactor power decrease leading to a positive fuel-induced reactivity feedback. The fuel temperature coefficient in ATOM is about -2.35 pcm/K at BOC. The variation of  $T_a$  is limited due to the strongly negative CTC.

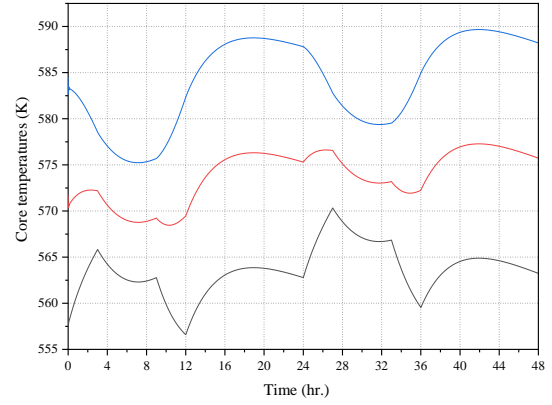


Fig. 5. Core coolant temperatures

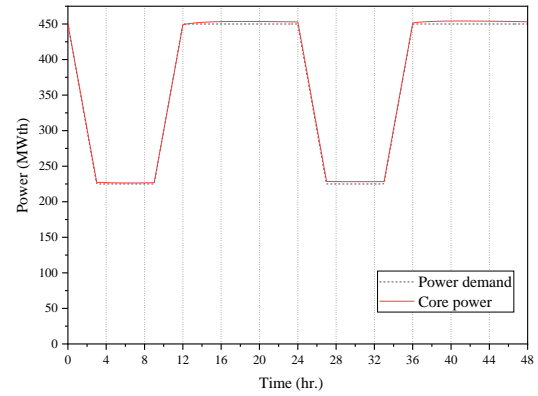


Fig. 6. Reactor power and power demand

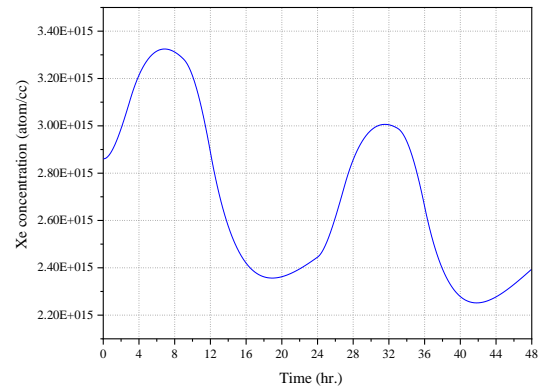


Fig. 7. Xe concentration variation

There is a big difference between the conventional programmed variation of coolant temperature with power and the autonomous variation that will be directly affected by Xe variation during the load-follow. However, it is easier to be understood as a widened dead-band for a constant  $T_a$  strategy. The variations of  $T_a$  must be accommodated by the reactor pressurizer. This is also requested in conventional constant inlet strategy where  $T_a$  changes by  $\sim 16$ K from HZP to HFP. It is worthwhile to mention that in an SMR with relatively large steam volume in the pressurizer such as SMART and relatively small primary coolant mass, such pressure variations will be noticeably smaller than in conventional large size PWRs. Figure 8 demonstrates the net reactivity obtained during the PCQM iterations. It is clear that the net

reactivity remains very close to the critically in the passive load-follow. It is just slightly negative during the power ramp-down phase and slightly positive at the power ramp-up phase. One of the key advantages of the proposed passively autonomous load-follow scheme in the SBF SMRs that it yields rather small deviations of the axial power shape and very small change in the radial power shape. This is especially important in comparison of the active load-follow operation using control rods, because the control rod adjustment clearly perturbs the axial and radial power profiles. Figures 9 and 10 show small changes of the 3-D fuel assembly power peaking and the axial shape index (ASI), respectively, during the passive load-follow simulation.

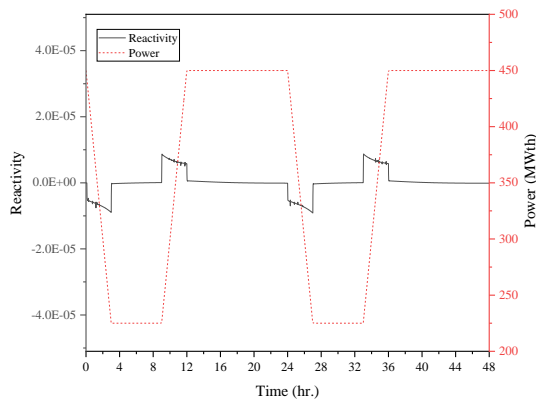


Fig. 8. Variation of the core reactivity

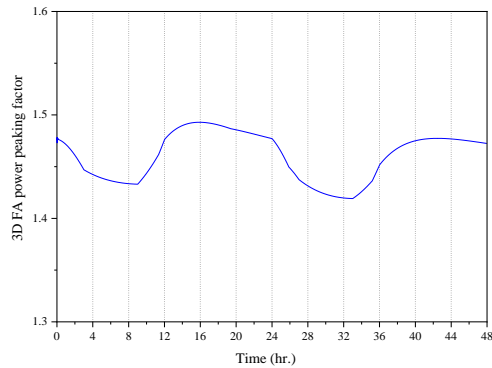


Fig. 9. 3-D Fuel assembly power peaking

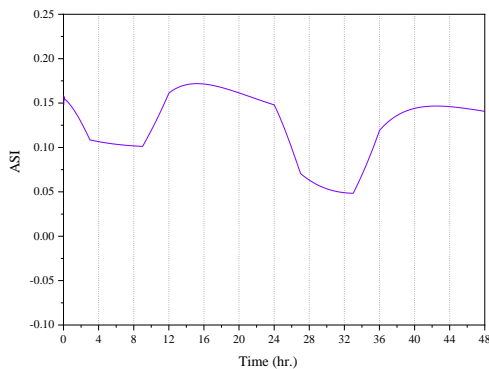


Fig. 10. ASI variation

Figure 11 shows the variation of the normalized axial power density distribution for selected time steps. It is clear that the variation is reasonably small. It is clearly affected by the variation of the inlet coolant temperature.

For example, after 30hr the relatively big variation of  $T_i$  leads to a balanced axial power distribution. The humps at the upper and the bottom of the core occur at the CSBA cutback regions [4].

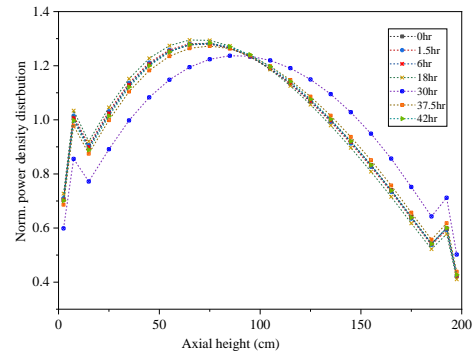


Fig. 11. Variation of the axial power distribution

#### 4. Conclusions

Time-dependent 3-D simulation was carried out for two days passively autonomous load-follow operation in the 450MWth SBF ATOM small PWR. A typically slow 100-50-100 load-pattern was studied. Confirming the results obtained previously using simple PK models, these results show the core power maneuvering is successfully governed by the natural  $T_i$  variation, and the deviation of  $T_a$  remains rather limited. The natural variation of  $T_i$  occurs due to extracting the demanded power from the primary loop. Moreover, it was found the ASI deviation and 3-D power peaking factors remain sufficiently small during the passively autonomous load-follow operation in ATOM.

#### ACKNOWLEDGEMENTS

The National Research Foundation of Korea (NRF) Grant funded by the Korean Government (MSIP) (NRF-2016R1A5A1013919) supported this work.

#### REFERENCES

1. Abdelhameed, A.A.E., K.S. Chaudri, and Y. Kim, *Three-D core multiphysics for simulating passively autonomous power maneuvering in soluble-boron-free SMR with helical steam generator*. Nuclear Engineering and Technology, 2020.
2. Abdelhameed, A.A.E., et al., *Feasibility of passive autonomous frequency control operation in a Soluble-Boron-Free small PWR*. Annals of Nuclear Energy, 2018. **116**: p. 319-333.
3. Abdelhameed, A.A.E. and Y. Kim, *Three-dimensional simulation of passive frequency regulations in the soluble-boron-free SMR ATOM*. Nuclear Engineering and Design, 2020: p. 110505.
4. Nguyen, X.H., A.A. Abdelhameed, and Y. Kim. *Optimization of centrally shielded burnable absorbers in soluble-boron-free SMR design*. in *Transactions of the Korean Nuclear Society Autumn Meeting, Gyeongju, Korea*. 2017.